Journal of ELECTRONIC MATERIALS, Vol. 41, No. 10, 2012
DOI: 10.1007/s11664-012-2122-6
© 2012 TMS

Study of Macrodefects in MBE-Grown HgCdTe Epitaxial Layers Using Focused Ion Beam Milling

M. REDDY,[1,2] J. WILDE,[1] J. M. PETERSON,[1] D.D. LOFGREEN,[1] and S.M. JOHNSON[1]

1.—Raytheon Vision Systems, 75 Coromar Dr., B-2/8, Goleta, CA 93117, USA. 2.—e-mail: Madhusudhana_reddy@raytheon.com

This paper presents a study on the initiation and evolution of macrodefects in molecular beam epitaxy-grown two-color HgCdTe epitaxial layers on CdZnTe substrates. A combination of focused ion beam milling and high-resolution scanning electron microscopy was used to look at the defect cross-sections, and energy-dispersive x-ray spectroscopy was used to study the cross-sectional composition. This study shows that the classic microvoids tend to initiate at interfaces, such as the substrate/epitaxial layer interface and *n*–*p* junctions, because of nonoptimum growth conditions. Another class of microvoids was traced to Te precipitates existing in CdZnTe substrates. Large circular defects, occasionally seen on HgCdTe epitaxial layers, were traced to a tiny volatile particle on the substrate, which is believed to be organic in nature. Another large, irregularly shaped Te-rich defect is seen initiating abruptly during growth and is attributed to occasional outburst of Te clusters from effusion cells.

Key words: HgCdTe, two color, dual band, molecular beam epitaxy (MBE), focused ion beam, scanning electron microscope

INTRODUCTION

Over the past few years, rapid progress has been made at Raytheon Vision Systems (RVS) in molecular beam epitaxy (MBE) growth of single- and multicolor HgCdTe detector structures on both Si and CdZnTe large-area substrates and in the demonstration of larger format focal-plane arrays.[1,2] As the demand for larger format and higher pixel density focal-plane arrays is constantly increasing and the performance requirements are becoming more stringent, there exists an unprecedented need to minimize the causes of pixel failure. One among many mechanisms that can cause pixel failure is the presence of macrodefects in the MBE-grown epitaxial HgCdTe layers. Macrodefects include both microvoids and voids and other larger defects, which can be seen on MBE-grown HgCdTe epitaxial layers under optical microscopy. In the past, many papers have reported the detrimental effect of macrodefects on pixel performance.[3–6] Notable among such efforts was a study on the effect of macrodefects on pixel operability of a long-wave infrared (LWIR) HgCdTe focal-plane array (FPA) of 256 × 256 format with 30 μm pixel pitch grown on (211)Si.[7] Prior to FPA fabrication, the exact location and size of the defects on the wafer were measured using an August NSX-105 system. A cross-correlation study was conducted between the pixel noise equivalent differential temperature (NEΔT) and the location of the nearby macrodefects. In this case, pixels showing NEΔT of more than two times the median NEΔT value were treated as inoperable pixels. The FPA median NEΔT was 29 mK. Figure 1a shows the location of inoperable pixels and the macrodefects on the FPA. The cross-correlation between the pixel inoperability and the location of the nearby defects is plotted in Fig. 1b. As shown in the plot, the cross-correlation analysis places each inoperable pixel at the center of the plot and marks the relative coordinates of nearby defects

(Received December 22, 2011; accepted April 27, 2012; published online May 31, 2012)

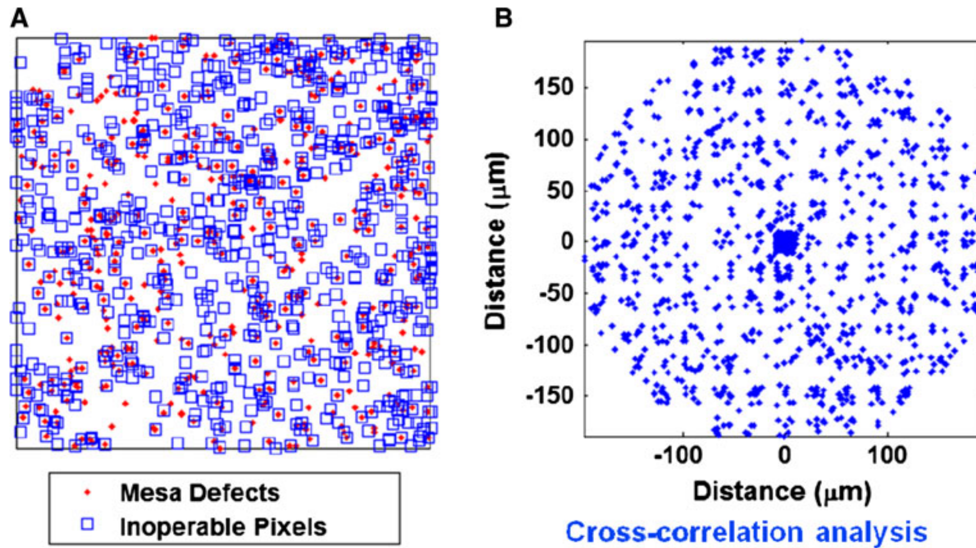

Fig. 1. (a) Coordinates of inoperable pixels and mesa defects. (b) Cross-correlation of inoperable pixels and neighboring macrodefects. From the dense square at the center of the plot, it is evident that there is a strong correlation between the inoperable pixels and the location of macrodefects.

within a radius of 200 μm. If every inoperable pixel has a defect inside the pixel then the cross-correlation plot should show a dense square at the center of the plot. In fact, such a dense square at the center is seen in Fig. 1b, indicating a strong correlation between the pixel operability and the macrodefects seen on the FPA.

Various types of defects on MBE-grown HgCdTe, such as misfit dislocations,[8] threading dislocations,[9] stacking faults and twins,[10,11] cross-hatch defects,[12–14] surface crater defects,[8,14] and void–hillocks,[15,16] as well as precipitates,[8] have been reported in literature. The defect terminology followed by various authors is unfortunately not common. Surface crater defects resemble more closely what we refer to in this report as voids. Pyramidal defects, sometimes also called void–hillock complexes or triangular defects, more closely resemble microvoids in this report. Many techniques, such as transmission electron microscopy,[8] high-resolution electron microscopy,[8] cross-sectional electron microscopy, atomic force microscopy,[10] Nomarski optical microscopy, and scanning electron microscopy (SEM),[15] have been used for study of macrodefects on MBE-grown HgCdTe. However, no comprehensive study using the focused ion beam (FIB) technique along with high-resolution SEM has been reported for cross-sectional study of macrodefects on HgCdTe; an exception was the study related to the defects on CdTe and CdSeTe.[17] In this paper, we present the results of our study on the origin and evolution of macrodefects in MBE-grown HgCdTe epitaxial layers on CdZnTe substrate using FIB milling, high-resolution scanning electron microscopy (HRSEM), and energy-dispersive x-ray spectroscopy (EDX). The goal is to obtain a better understanding of defect pedigree to allow a reduction in the defect density by making appropriate modifications to the growth conditions.

EXPERIMENTAL PROCEDURES

A 10-inch VG Semicon V-100 MBE system was used for HgCdTe growth on CdZnTe (211)B substrates. The system has ZnTe, CdTe, and Te solid sources, a liquid Hg source for HgCdTe growth, and In and As for *n*-type and *p*-type doping, respectively. For more details about the MBE growth procedure, the reader is referred to our previous paper.[18] In this study, data are presented for two-color *n*–*p*–*n* triple-layer heterojunction (TLHJ) structures. Figure 2 shows the whole-wafer defect histogram using the automated August NSX-105 system for one of the *n*–*p*–*n* layers used in this study. From the figure, it is clear that the bulk of the defects belong to the first three bins, namely the 0 μm to 3 μm, 3 μm to 6 μm, and 6 μm to 9 μm bins. These defects are mostly of regular shape and fall into the category of microvoids; one representative defect from each bin was selected for FIB study. The void defect density on these wafers is very low, and therefore no study was undertaken on these defects. There appears to be a reasonable consensus among scientific community as to the nature and manifestation of these void (crater) defects.[8,14,15] Void defects are generally irregular in shape and can grow to several microns in size depending on the growth conditions. They are initiated under Te-rich or elevated growth temperature conditions or due to substrate surface contamination. The other category of defects studied were large defects that belong to >15 μm bin. They look very distinct from voids, and elimination of these defects is very important because they can potentially cause cluster outages on FPAs.

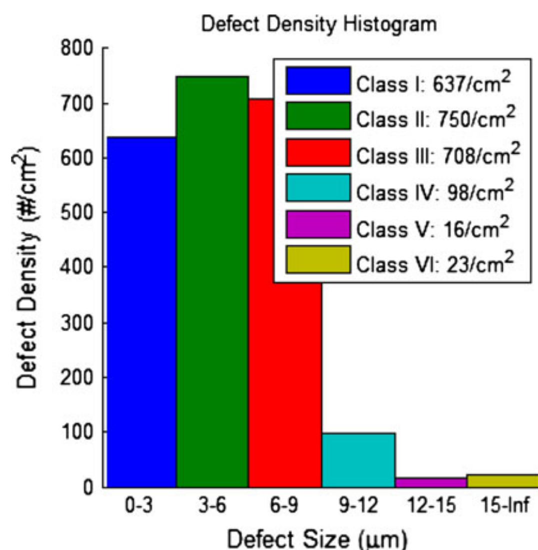

Fig. 2. Whole-wafer histogram of defects on TLHJ HgCdTe on CdZnTe. The defect density of each bin may vary depending on growth conditions.

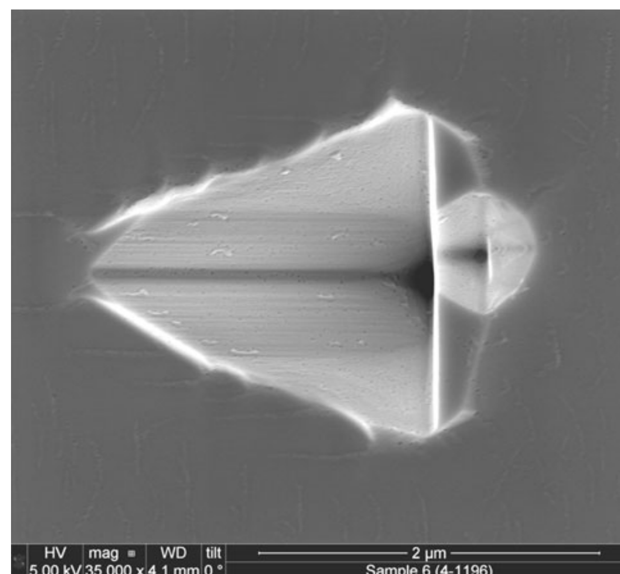

Fig. 3. SEM image of a microvoid of size around 2 μm.

The cross-sectional defect study was done using a FEI DB235 dual-beam FIB system at the Material Research Laboratory, University of California at Santa Barbara. The DB235 includes both HRSEM and FIB. HRSEM uses a Schottky emitter to enable resolution of 3 nm, and the FIB system, with a liquid Ga metal ion source, is capable of 7 nm resolution. An in-house EDX was used for cross-sectional composition analysis.

RESULTS AND DISCUSSION

Figure 3 shows a plan view of a microvoid of size around 2 μm, which belongs to the 0 μm to 3 μm bin. This defect has the shape of an irregular tetrahedron with faceted walls and makes an isosceles triangle when it intersects the growth surface. There is a void space inside the defect and a hole at the vortex of the tetrahedron. The faceted walls of the defect rise above the plane of the epitaxial layer, and the wall on the right side (the base of the isosceles triangle) has a larger elevation. From the figure, it can also be seen that another small microvoid of similar shape nucleated at the right side-wall of the defect. Similar microvoids have been reported on HgTe and HgCdTe in literature.[16] The faceted wall with larger elevation was attributed to the step flow direction of the epitaxial layer growth. The shape of such faceted microvoids on HgCdTe surfaces was reported to be growth temperature dependent; the shape changes from diamond to triangle when the growth temperature is varied from a few degrees below the optimum value to a few degrees above the optimum value, respectively.[16] An increase in etch pit density (EPD) was reported for growth temperatures lower than the optimum value, and an increase in the void density was reported at higher growth temperatures.[5] We believe that the growth temperature for the epitaxial layers used in this study was very close to or slightly lower than the optimum growth temperature, because an increase in neither EPD nor void defect density was noticed on the layers grown under similar conditions. Figure 4 shows the FIB cross-section of the defect just before the origin of the defect was revealed. Figure shows a few void spaces along the line beginning from the hole at the vortex to probably the origin of the defect, and we call this a void pipe. Also, it can be seen that the direction of defect propagation is inclined, by roughly 16°, to the [211] growth direction. It was reported earlier that microvoids are associated with the formation of microtwins, which can be generated due to a high Hg/Te flux ratio, low growth temperature, or due to the presence of surface impurities.[8,11] The defects caused by these microtwins would prefer to grow off-angle to the [211] growth direction.[8,11] Figure 5 reveals the true power of the combination of FIB and HRSEM in tracing the origin of these microvoids. As one can see from the figure, this particular microvoid is generated at the *n*–*p* junction. The growth conditions at this interface are far from steady state, as several changes, e.g., in the composition, growth temperature, and Hg flux, and the initiation of As flux, take place at this interface. These changes, if not controlled carefully, can provide right conditions for the initiation of these microvoids.

Figure 6 shows an SEM picture of a microvoid from the 3 μm to 6 μm defect bin. This defect is 4 μm in size and encompasses several microvoids similar to those shown in Fig. 4. Each of these microvoids is surrounded by faceted walls and void space inside them. A void pipe can also be seen at the vertex of the faceted walls, going deep inside of each defect. As the FIB milling progressed through the defect,

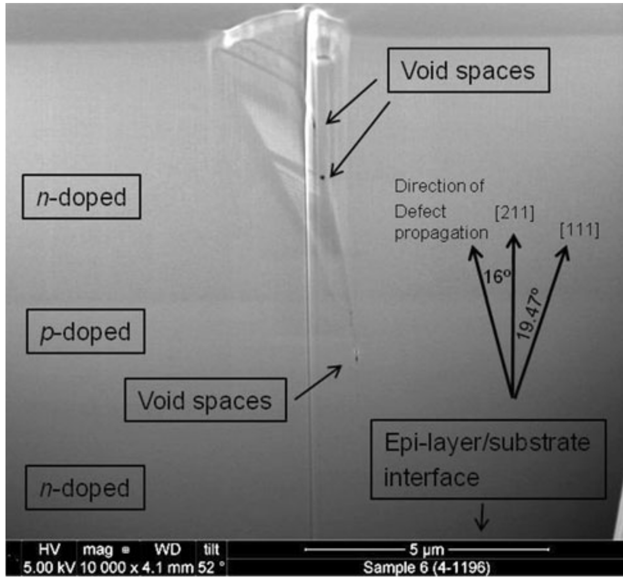

Fig. 4. FIB cross-section of a microvoid. Several void spaces are seen inside the defect.

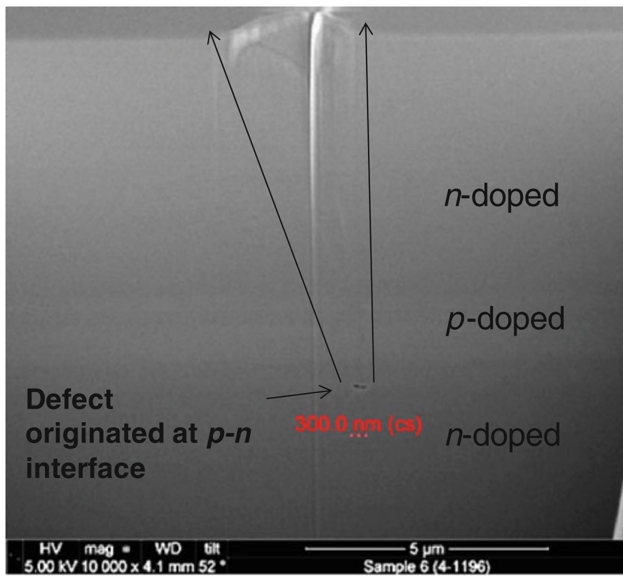

Fig. 5. FIB cross-section of a microvoid. Defect is originated at the interface of *n*-doped and *p*-doped layers.

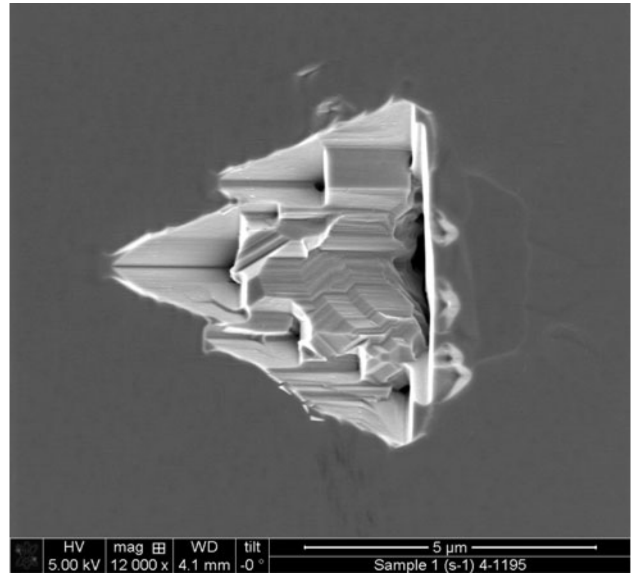

Fig. 6. SEM image of a microvoid.

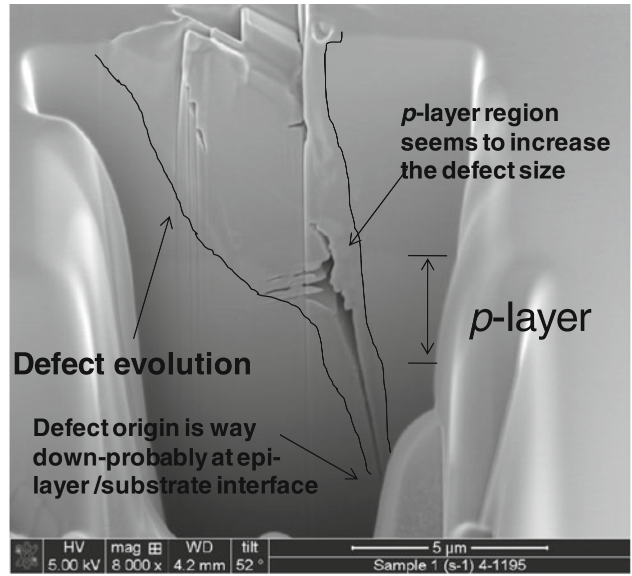

Fig. 7. FIB cross-section of a microvoid.

the void pipes of several small microvoids in this defect were exposed until we reached the center of the defect, where the main void pipe leading to the defect origin is revealed as shown in Fig. 7. In this image, the exact defect origin is unfortunately concealed because of an obstruction. However, as one can see from this image, the defect was initiated either at or very close to the substrate/epitaxial layer interface. The defect size remains very small, mainly consisting of void space with no faceted growth inside, throughout the initial n-type layer. In contrast, the progression of the microvoid shown in Fig. 4 is relatively faster, with the presence of both void space and faceted growth. As is evident from Fig. 7, the defect size becomes abruptly larger at the growth transition from the n-type to p-type layer, probably due to nucleation of additional microvoids. The changes in the growth conditions at this interface may have aided the nucleation of additional microvoids around the original defect. Finally, it can also be seen here that the defect growth direction is inclined at an angle to the epitaxial layer growth direction, suggesting the association of microtwins with this defect formation.

Figure 8 shows a relatively larger microvoid of size approximately 7 μm, which belongs to the 6 μm to 9 μm defect bin. This microvoid has several distinct features compared with the other two defects mentioned above. This defect still has a triangular

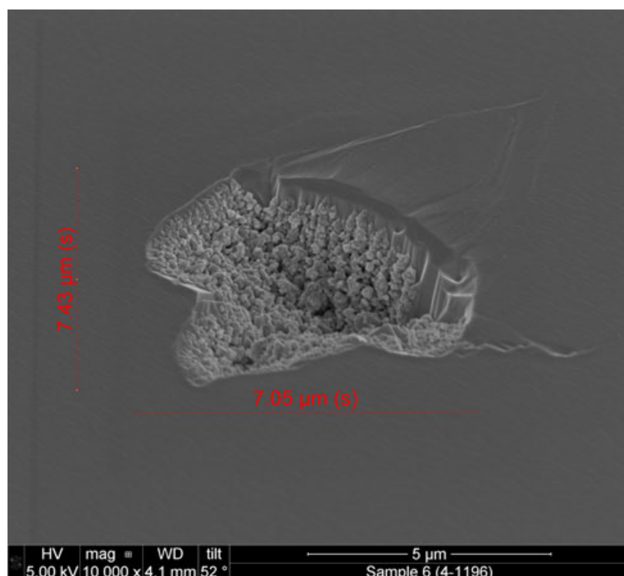

Fig. 8. SEM image of a microvoid.

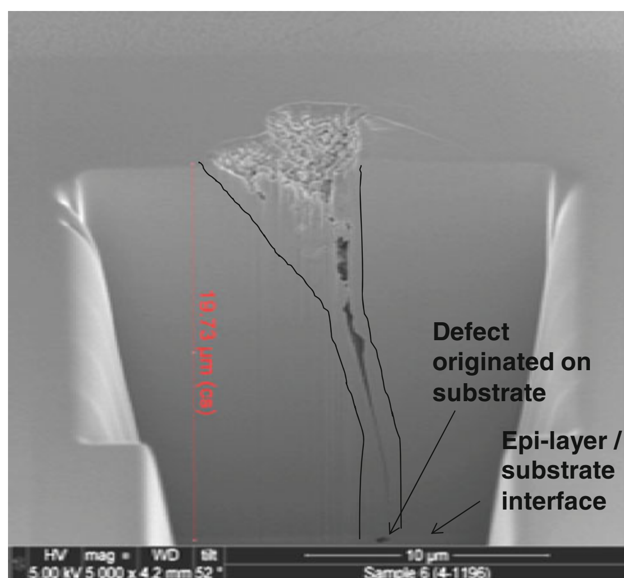

Fig. 9. FIB cross-section of a microvoid. The defect is caused by an object, probably a Te precipitate, native to the CdZnTe substrate.

shape, though distorted to a large extent. It appears to have amorphous-type material growth inside the defect. The defect walls are faceted to a lesser degree, and no additional microvoids are seen around this defect. It was noticed that the density of these defects is less dependent on moderate changes in growth conditions. An FIB cross-sectional SEM image of this defect is shown in Fig. 9. It is very clear that the defect is caused by an object lying just beneath the substrate surface. This object is likely to be a Te precipitate. This explains why the density of these defects seems not to depend on the growth conditions. A similar observation was made earlier on Te precipitate-related HgCdTe defects on

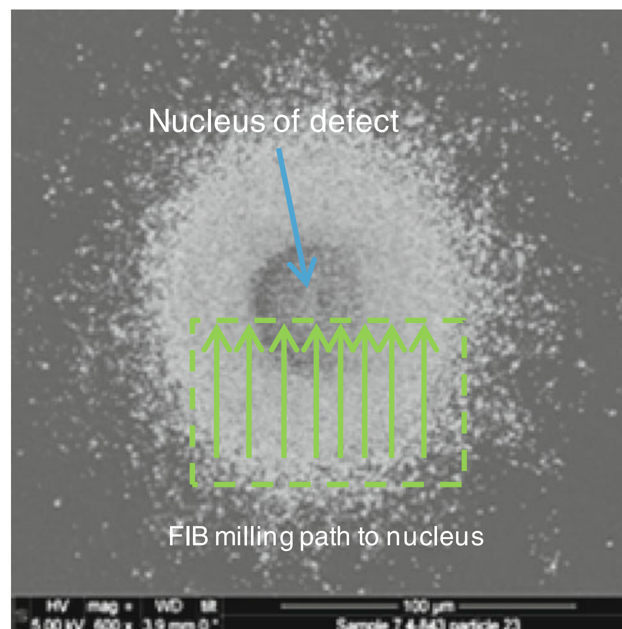

Fig. 10. Large circular defect with a nucleus at the center. Also seen is the FIB milling path starting from the defect periphery to the center.

CdZnTe substrates.[19] The density of these defects reduced considerably when low-Te-precipitate CdZnTe substrates were used.[19] There is also a considerable difference in the defect evolution when compared with the two microvoids discussed above. For the first few microns of growth, the direction of defect growth and the epitaxial layer growth remain the same; then, as the growth proceeds further, the defect growth direction deviates in just the same way as seen with the earlier two defects.

Figure 10 shows one of the larger circular defects of approximately 100 μm diameter that we occasionally see on HgCdTe epitaxial layers. This defect, unlike other defects, is coplanar with the epitaxial layer surface, except for a small portion at the center, which is slightly elevated; this portion is marked as nucleus in the figure. As shown in Fig. 11, FIB milling was started at the periphery of the defect and slowly approached towards the nucleus. Away from the nucleus, some void spaces are seen, particularly in the *p*-layer, indicating the poor quality of the epitaxial layer. At the nucleus, the source of the defect is revealed as a small particle that is a few nanometers wide, as shown in Fig. 12. EDX was attempted to study the composition of the particle, but with no success due to its extremely small size. After several minutes of probing with the EDX, the particle evaporated. This particle is believed to be volatile organic matter in nature, and the large circular defect surrounding this particle may have been caused by pregrowth excessive outgassing of this particle.

Figure 13 shows another large defect, again occasionally seen on HgCdTe epitaxial layers, of random shape and slightly elevated above the plane

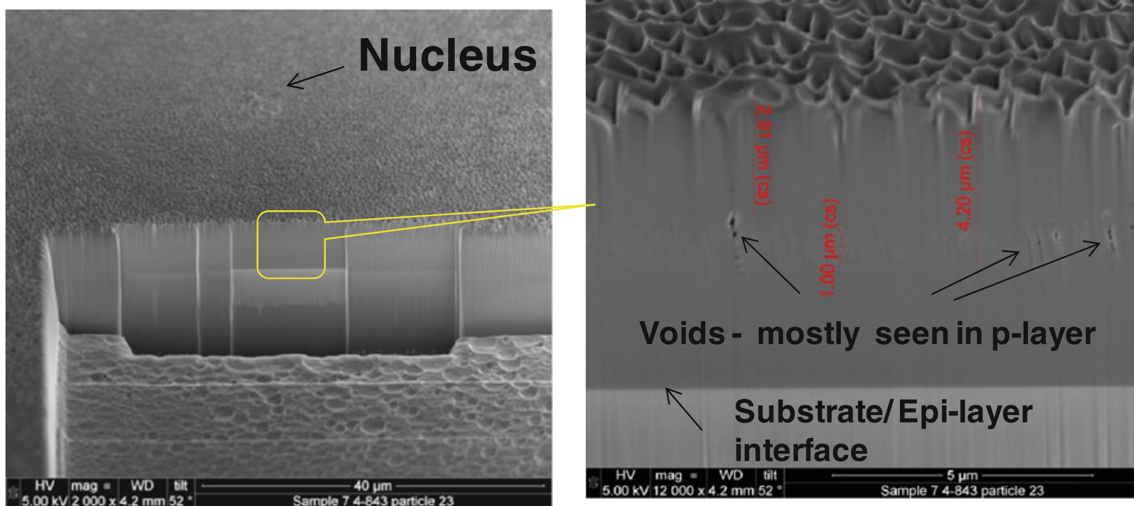

Fig. 11. SEM image of a partly uncovered defect cross-section by FIB. On the right is the magnified image showing the poor epitaxial layer quality with void spaces.

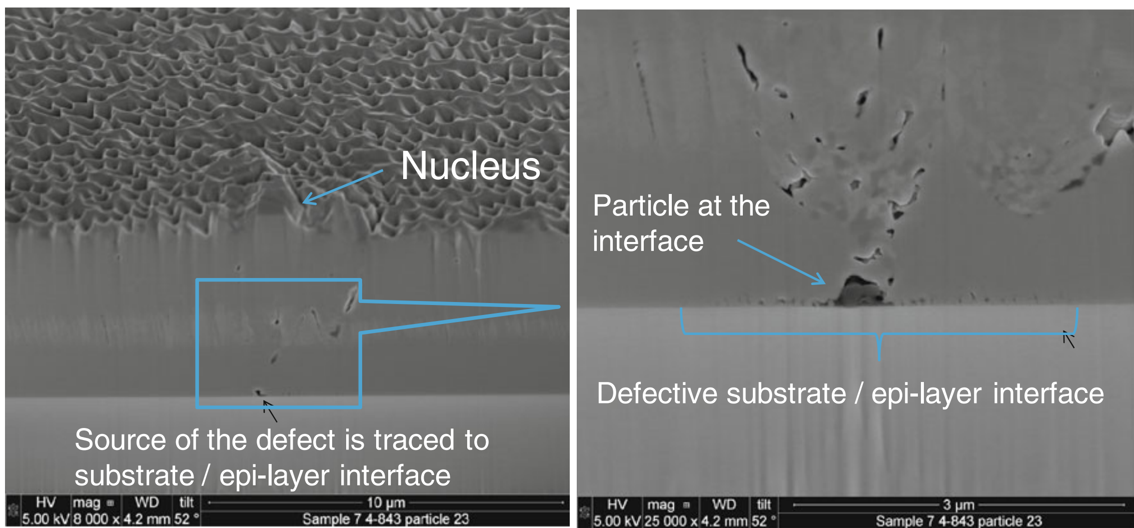

Fig. 12. SEM image of defect cross-section, revealing the source of the defect as a small particle. On the right is a magnified image of the small particle that caused this huge defect of about 100 μm diameter.

of the epitaxial layer surface. FIB milling successfully exposed the origin of this defect, as seen in Fig. 14. This defect originates abruptly during the growth, about 13 μm from the epitaxial layer/substrate interface, and is quite porous in nature. EDX analysis (Table I) shows elevated Te and reduced Cd and Hg at two locations on the defect cross-section. This result suggests that the defect was most likely caused by arrival of a cluster from the Te effusion cell during the growth. The presence of Cd and Hg in this defect can be explained by the porous nature of the defect, and Cd and Hg may have diffused into the defect during several microns of HgCdTe growth after the cluster landing on the growth surface.

CONCLUSIONS

Classic microvoids with faceted walls and void pipes appear to initiate at interfaces such as the substrate/epitaxial layer interface and n-doped/p-doped layer interfaces. They most likely are initiated because of microtwin formation due to rather abrupt changes in growth conditions at these interfaces and, as a result, grow off-angle to the growth direction. After initiation, if the growth conditions are optimum, as they are during the n-doped layer growth in Fig. 7, the microvoid size remains small even after several microns of growth and mainly consists of a void pipe with no faceted

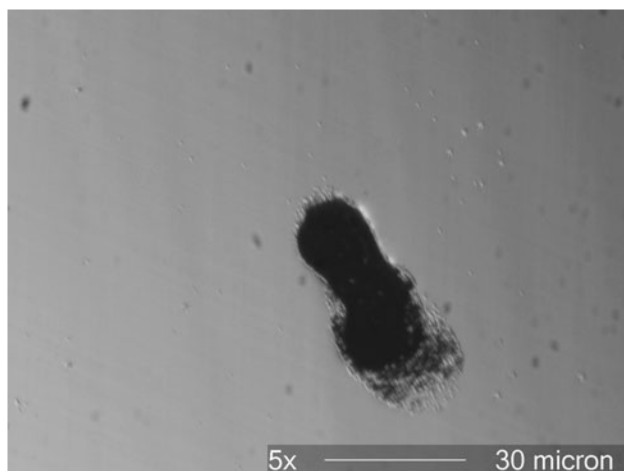

Fig. 13. Optical microscope picture of a larger, irregularly shaped defect.

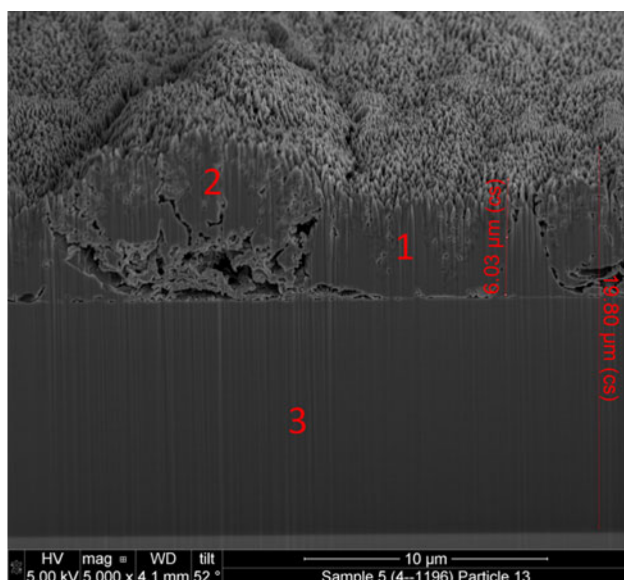

Fig. 14. FIB cross-section of a section of a large, irregularly shaped defect. Also marked on the figure are the locations of EDX study.

Table I. Atomic concentrations of Cd, Te, and Hg at various locations on the defect cross-section

Spot	Location	Cd (%)	Hg (%)	Te (%)
1	Defect area	10.5	33.6	55.1
2	Defect area	10.7	28.0	58.4
3	Nondefect area	12.2	37.8	50.0

A correction to the EDX concentrations was applied based on the atomic concentrations obtained by the secondary-ion mass spectroscopy depth profile at a nondefect location.

growth. On the other hand, if the growth conditions deviate from the optimum conditions, as they apparently do during the *p*-layer growth in both Figs. 4 and 7, the microvoid grows faster, with both void pipe and faceted growth inside the defect. Also, these nonoptimum growth conditions favor nucleation of additional microvoids inside and surrounding the original microvoid, as shown in Figs. 3 and 6. There is another class of microvoids, as shown in Fig. 8, with distinct features, such as distorted triangular shape and wall faceting with amorphous-type material growth inside the defect. Evolution of this microvoid is also different for the first few microns of growth, as the direction of defect growth coincides with that of epitaxial layer growth during this stage. The origin of this defect is attributed to Te precipitates in the CdZnTe substrates. This paper also reveals the reasons behind the formation of large defects that are occasionally seen on the HgCdTe layers. The large circular defect is believed to be caused by outgassing of tiny volatile organic particles on the substrate, and the random-shaped large defects are caused by the arrival of Te clusters from the effusion cell during the growth.

REFERENCES

1. D.J. Gulbransen, S.H. Black, A.C. Childs, C.L. Fletcher, S.M. Johnson, W.A. Radford, G.M. Venzor, J.P. Sienicki, A.D. Thompson, J.H. Griffith, A.A. Buell, M.F. Vilela, and M.D. Newton, *Proc. SPIE* 5406, 305 (2004).
2. E.P.G. Smith, G.M. Venzor, A.M. Gallagher, M. Reddy, J.M. Peterson, D.D. Lofgreen, and J.E. Randolph, *J. Electron. Mater.* 40, 1630 (2011).
3. J.B. Varesi, A.A. Buell, J.M. Peterson, R.E. Bornfreund, M.F. Vilela, W.A. Radford, and S.M. Johnson, *J. Electron. Mater.* 32, 667 (2003).
4. P.S. Wijewarnasuriya, M. Zandian, D.B. Young, J. Waldrop, D.D. Edwall, W.V. McLevige, D. Lee, J. Arias, and A.I. D'souza, *J. Electron. Mater.* 28, 649 (1999).
5. J.M. Arias, M. Zandian, J. Bajaj, J.G. Pasko, L.O. Bubulac, S.H. Shin, and R.E. De Wames, *J. Electron. Mater.* 24, 521 (1995).
6. C.A. Billman, L.A. Almeida, P. Smith, J.M. Arias, A. Chen, D. Lee, and E.C. Piquette, *J. Electron. Mater.* 40, 1693 (2011).
7. D.D. Lofgreen, M.F. Vilela, Y. Thai, and S.M. Johnson, Presented at *US Workshop on the Physics and Chemistry of II-VI Materials*, Baltimore, USA (2007).
8. T. Aoki, Y. Chang, G. Badano, J. Zhao, C. Grein, S. Sivananthan, and D.J. Smith, *J. Cryst. Growth* 265, 224 (2004).
9. J.R. Yang, X.L. Cao, Y.F. Wei, and L. He, *J. Electron. Mater.* 37, 1241 (2008).
10. I.V. Sabinina, A.K. Gutakovsky, Yu.G. Sidorov, and A.V. Latyshev, *J. Cryst. Growth* 274, 339 (2005).
11. R.J. Koestner and H.F. Schaake, *J. Vac. Sci. Technol. A* 6, 2834 (1988).
12. M. Martinka, L.A. Almeida, J.D. Benson, and J.H. Dinan, *J. Electron. Mater.* 31, 732 (2002).
13. D.R. Rhiger, J.M. Peterson, R.M. Emerson, E.E. Gordon, S. Sen, Y. Chen, and M. Dudley, *J. Electron. Mater.* 27, 615 (1998).
14. Y. Chang, C.R. Becker, C.H. Grein, J. Zhao, C. Fulk, T. Cassellman, R. Kiran, X.J. Wang, E. Robinson, S.Y. An, S. Mallick, S. Sivananthan, T. Aoki, C.Z. Wang, D.J. Smith, S. Velicu, J. Zhao, J. Crocco, Y. Chen, G. Brill, P.S. Wijewarnasuriya, N. Dhar, R. Sporken, and V. Nathan, *J. Electron. Mater.* 37, 1171 (2008).

15. D. Chandra, F. Aqariden, J. Frazier, S. Gutzler, T. Orent, and H.D. Shih, *J. Electron. Mater.* 29, 887 (2000).
16. E. Selvig, C.R. Tonheim, T. Lorentzen, K.O. Kongshaug, T. Skauli, and R. Haakennasen, *J. Electron. Mater.* 37, 1444 (2008).
17. E.M. Campo, T. Hierl, J.C.M. Hwang, Y. Chen, and G. Brill, *J. Electron. Mater.* 34, 953 (2005).
18. M. Reddy, J.M. Peterson, T. Vang, J.A. Franklin, M.F. Vilela, K. Olsson, E.A. Patten, W.A. Radford, J.W. Bangs, L. Melkonian, E.P.G. Smith, D.D. Lofgreen, and S.M. Johnson, *J. Electron. Mater.* 40, 1706 (2011).
19. E.C. Piquette, M. Zandian, D.D. Edwall, and J.M. Arias, *J. Electron. Mater.* 30, 627 (2001).